Complex Slip Distribution of the 2021 M_w 7.4 Maduo, China, Earthquake: An Event Occurring on the Slowly Slipping Fault

Rumeng Guo[1,2], Hongfeng Yang[*2,3], Yu Li[4,5], Yong Zheng[6], and Lupeng Zhang[7,8]

Abstract

The 21 May 2021 Maduo earthquake occurred on the Kunlun Mountain Pass–Jiangcuo fault (KMPJF), a seismogenic fault with no documented large earthquakes. To probe its kinematics, we first estimate the slip rates of the KMPJF and Tuosuo Lake segment (TLS, ~75 km north of the KMPJF) of the East Kunlun fault (EKLF) based on the secular Global Positioning System (GPS) data using the Markov chain Monte Carlo method. Our model reveals that the slip rates of the KMPJF and TLS are 1.7 ± 0.8 and 7.1 ± 0.3 mm/yr, respectively. Then, we invert high-resolution GPS and Interferometric Synthetic Aperture Radar observations to decipher the fault geometry and detailed coseismic slip distribution associated with the Maduo earthquake. The geometry of the KMPFJ significantly varies along strike, composed of five fault subsegments. The most slip is accommodated by two steeply dipping fault segments, with the patch of large sinistral slip concentrated in the shallow depth on a simple straight structure. The released seismic moment is $\sim 1.5 \times 10^{20}$ N·m, equivalent to an M_w 7.39 event, with a peak slip of ~9.3 m. Combining the average coseismic slip and slip rate of the main fault, an earthquake recurrence period of $\sim 1250^{+1120}_{-400}$ yr is estimated. The Maduo earthquake reminds us to reevaluate the potential of seismic gaps where slip rates are low. Based on our calculated Coulomb failure stress, the Maduo earthquake imposes positive stress on the Maqin–Maqu segment of the EKLF, a long-recognized seismic gap, implying that it may accelerate the occurrence of the next major event in this region.

Cite this article as Guo, R., H. Yang, Y. Li, Y. Zheng, and L. Zhang (2021). Complex Slip Distribution of the 2021 M_w 7.4 Maduo, China, Earthquake: An Event Occurring on the Slowly Slipping Fault, *Seismol. Res. Lett.* **XX**, 1–13, doi: 10.1785/0220210226.

Supplemental Material

Introduction

The continuous convergence between the Eurasian and Indian plates in the past ~50 Ma results in crust thickening and rapid uplift of the Tibetan plateau (e.g., Yin and Harrison, 2000). Accompanying the growth of the plateau, lateral extrusion of the Asian lithosphere has been suggested along major strike-slip faults (e.g., England and Houseman, 1986). The northeast margin of the Tibetan plateau is characterized by a series of nearly parallel northwest–southeast-trending strike-slip faults, including the ~1600-km-long left-lateral East Kunlun fault (EKLF) that divides the margin into the Qaidam block to the north and the Bayan Har block to the south. The EKLF consists of several major segments, from west to east, the Kusai Lake segment, Xidatan–Dongdatan segment, Alake Lake segement, Tuosuo Lake segment (TLS), and Maqin–Maqu segment (MMS) (Fig. 1, Ryder *et al.*, 2011).

Since the end of the twentieth century, all large earthquakes $M \geq 7$) in China have occurred on faults surrounding the Bayan Har block (Fig. 1), including the 2001 M_w 7.8 Kokoxili earthquake in the northern boundary (Zhao *et al.*, 2021); the 1996 M_s 7.1 Karakoram Pass earthquake (Qiu *et al.*, 2019), the 1997 M_w 7.5 Manyi earthquake (Wen and Ma, 2010), and the 2010 M_s 7.1 Yushu earthquake (Li, Elliott, *et al.*, 2011) along the southern border; two M_s 7.3 Yutian earthquakes in 2008 and 2014, respectively, at the western margin (Furuya

1. State Key Laboratory of Geodesy and Earth's Dynamic, Innovation Academy for Precision Measurement Science and Technology, Chinese Academy of Sciences, Wuhan, China; 2. Earth System Science Programme, The Chinese University of Hong Kong, Shatin, Hong Kong, China, https://orcid.org/0000-0002-5925-6487 (HY); 3. Shenzhen Research Institute, The Chinese University of Hong Kong, Shenzhen, Guangdong, China; 4. Institute of Geophysics, China Earthquake Administration, Beijing, China, https://orcid.org/0000-0001-6733-5057 (YL); 5. China Earthquake Networks Center, China Earthquake Administration, Beijing, China; 6. State Key Laboratory of Geological Processes and Mineral Resources, Institute of Geophysics and Geomatics, China University of Geosciences, Wuhan, China, https://orcid.org/0000-0001-6157-8584 (YZ); 7. Faculty of Geosciences and Environmental Engineering, Southwest Jiaotong University, Chengdu, China, https://orcid.org/0000-0003-3358-8018 (LZ); 8. Division of Geodetic Science, School of Earth Science, Ohio State University, Columbus, Ohio, U.S.A.

*Corresponding author: hyang@cuhk.edu.hk

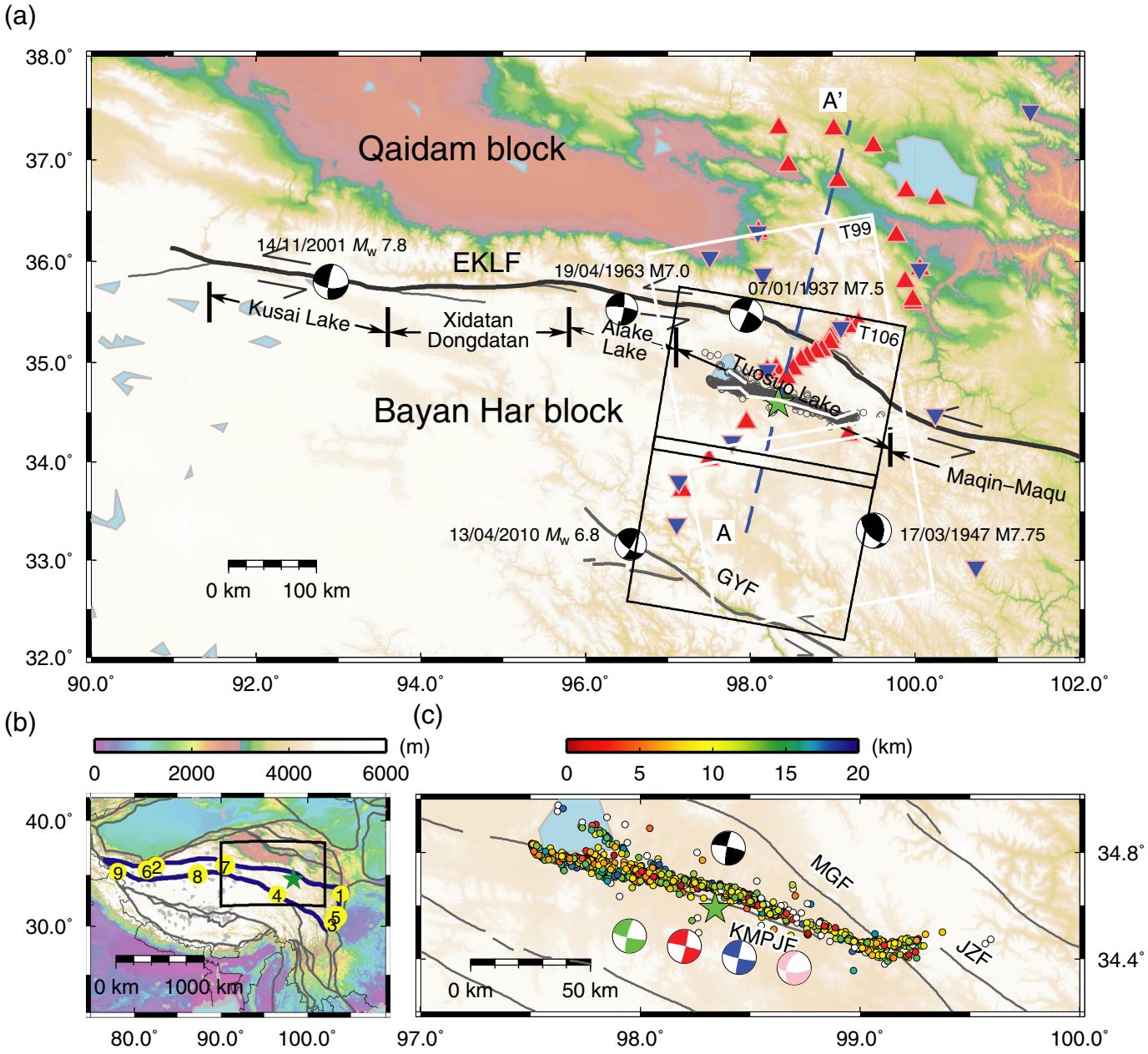

Figure 1. Tectonic setting of the 2021 Maduo earthquake. (a) Seismogenic environment of the Maduo event and geodetic data sets used in this article. Green star represents the epicenter of the Maduo earthquake from the China Earthquake Networks Center (CENC) catalog. Black focal mechanism plots indicate the focal mechanisms of major historical earthquakes near the Maduo source region (Shan *et al.*, 2015). Blue and red triangles represent the Global Positioning System (GPS) stations that captured the coseismic and interseismic secular deformation, respectively. White lines denote our optimal fault traces. (b) Seismicity near the Bayan Har block. Blue curves outline the borders of the Bayan Har block. Yellow circles are the historical earthquakes since the 1990s from the U.S. Geological Survey (USGS) catalog. The black rectangle outlines our studied region. (c) Relocated aftershock distribution. The relocated aftershocks occurred within 8 days after the mainshock from the work of Wang, Fang, *et al.* (2021). Green, red, blue, and pink focal mechanism plots denote the focal mechanisms associated with the Maduo earthquake from the CENC, Global Centroid Moment Tensor (Global CMT), GeoForschungsZentrum (GFZ), and USGS catalogs, respectively. The black focal mechanism plot represents the focal mechanism based on our preferred slip model. 1, 2017 M_S 7.0 Jiuzhaigou earthquake; 2, 2014 M_S 7.3 Yutian earthquake; 3, 2013 M_S 7.0 Lushan earthquake; 4, 2010 M_S 7.1 Yushu earthquake; 5, 2008 M_S 8.0 Wenchuan earthquake; 6, 2008 M_S 7.3 Yutian earthquake; 7, 2001 M_W 7.8 Kokoxili earthquake; 8, 1997 M_W 7.5 Manyi earthquake; 9, 1996 M_S 7.1 Karakoram Pass earthquake. T99, ascending track 99; T106, descending track 106. EKLF, East Kunlun fault; GYF, Ganzi–Yushu fault; JZF, Jiuzhi fault; KMPJF, Kunlun Mountain Pass-Jiangcuo fault; MGF, Maduo–Gande fault. The color version of this figure is available only in the electronic edition.

and Yasuda, 2011; Li *et al.*, 2016); and the 2008 M_s 8.0 Wenchuan earthquake (Shen *et al.*, 2009), the 2013 M_s 7.0 Lushan earthquake (Jiang *et al.*, 2014), and the 2017 M_s 7.0 Jiuzhaigou earthquake (Tang *et al.*, 2021) in the eastern rim. Furthermore, Wen *et al.*, (2011) found that eight major historical events had ruptured approximately two-third of its northern boundary, and it was characterized by accelerating stress release and gradually shortening seismic intervals. Thus, they suggested that the northern boundary had a high likelihood of hosting a large earthquake in the near future.

On 22 May 2021 at 02:04 Beijing Standard Time (UTC 21 May 2021 18:04), an M_w 7.4 earthquake struck the northern boundary of the Bayan Har block. However, it did not occur on the EKLF but on the Kunlun Mountain Pass–Jiangcuo fault (KMPJF), a branch fault that has received little attention and is located about 75 km south of the TLS of the EKLF (Fig. 1). Because this event occurred in the vicinity of Maduo county of Golog Tibetan autonomous prefecture in the Qinghai Province, hereafter, it is named the Maduo earthquake. The Maduo earthquake ruptured a ~170-km-long fault zone with low-background seismicity (Wen *et al.*, 2007; Wang, Fang, *et al.*, 2021) and further verified that the Bayan Har block is prone to strong earthquakes. Therefore, probing the source characteristics of the Maduo event is helpful for understanding strong earthquakes in this region, which is of great significance to further analyzing the seismogenic mechanism and dynamic process.

The 2021 Maduo earthquake caused very strong shaking in the surrounding areas, with the highest intensity of X (Wang, Fang, *et al.*, 2021). Fortunately, this event occurred in no man's land and caused no casualties. The hypocenter estimated by the China Earthquake Networks Center (CENC) is located at 34.59° N, 98.34° E at a depth of 17 km (see Data and Resources), which is about 9 km east of the location reported by the U.S. Geological Survey (USGS) National Earthquake Information Center (34.61° N, 98.25° E, 10 km; see Data and Resources). The focal mechanism from the Global Centroid Moment Tensor (Global CMT) catalog suggests that the Maduo earthquake is dominated by the sinistral movements with minor normal components on the fault-plane striking N103°W and dipping 87° to the northeast (see Data and Resources). The GeoForschungsZentrum (GFZ) solution has a similar pattern to the Global CMT (strike: 102°, dip: 84°, rake: −3°), but dips to the southwest (see Data and Resources). In addition, the centroid moment solution from USGS indicates a sinistral component with a rake angle of -40°, revealing a significant normal component, and a shallower dip of 67° with a strike of 92° is reported (Fig. 1c). These significant differences in earthquake locations and focal mechanisms may be attributed to different seismic data and inversion strategies. Near-field geodetic observations not only untie the interseismic kinematic status of faults but also provide unprecedented constraints on the detailed fault geometry and coseismic deformation, thus improving the accuracy of source parameters and our understanding of seismic hazard.

In this article, we first estimate the slip rates of KMPJF and TLS of the EKLF using the Markov chain Monte Carlo (MCMC) method and then invert the detailed coseismic slip distribution of the 2021 Maduo event using the steepest descent method based on the high-quality geodetic measurements. Finally, we discuss the tectonic implications of the Maduo earthquake on the future seismic hazard assessment.

Data, Methodology, and Model Configuration

Secular kinematic model

Elastic dislocation model. Interseismic deformation along a long, straight strike-slip fault is usually attributed to uniform aseismic slip at depth on the fault, that is, the fault is replaced by a vertical elastic cut, and continuous slip occurs below the interseismic locking depth H at slip rate V. In the simple conventional model of strain accumulation (Savage and Burford, 1973), the fault-parallel surface velocity v is related to the horizontal distance to the fault trace x:

$$v(x) = \frac{V}{\pi}\arctan\left(\frac{x}{H}\right). \tag{1}$$

This model has been widely used to estimate the fault-locking depth and slip rate (e.g., Guo *et al.*, 2018; Diao *et al.*, 2019). In this article, given that the Maduo earthquake occurred on the KMPJF instead of the rapidly deforming TLS ~75 km to the north, we need to combine the effects of these two faults simultaneously. According to the linear elastic dislocation theory, we linearly superimpose their contributions (Zhu *et al.*, 2021); at this time, the velocity parallel to the fault (v) is expressed by

$$v(x) = \frac{V_1}{\pi}\arctan\left(\frac{x_1}{H_1}\right) + \frac{V_2}{\pi}\arctan\left(\frac{x_2}{H_2}\right)\cos\theta + \text{alpha}, \tag{2}$$

in which V_1 and V_2 represent the slip rates of the KMPJF and TLS, respectively. x_1 and x_2 are the distances from Global Positioning System (GPS) stations to the fault traces of KMPJF and TLS, respectively. H_1 and H_2 denote the locking depths of these two faults, respectively. θ is the angle between these two fault traces, which is about 10° here. alpha is a static constant offset between the observed and modeled velocities (e.g., Aslan *et al.*, 2019).

MCMC method. The optimal model parameters are estimated using the MCMC Bayesian method. The nonlinear functional relationship between the data $\boldsymbol{d}$ and model parameters $\boldsymbol{m}$ is defined by (Johnson and Segall, 2004)

$$\mathbf{d} = g(\mathbf{m}). \tag{3}$$

The posteriori probability density function (PDF) of the model parameters σ is expressed as follows (Mosegaard and Tarantola, 2002; Johnson and Segall, 2004):

$$\sigma(\mathbf{m}|\mathbf{d} = g(\mathbf{m})) = k\rho_M(\mathbf{m})\rho_D(g(\mathbf{m})), \quad (4)$$

in which k represents a normalization constant called marginal likelihood, which ensures that the posterior integrates to 1. ρ_M and ρ_D denote the priori PDF for the model parameters and the PDF of the model parameters given only the information from the data, respectively (e.g., Mosegaard and Tarantola, 2002). To gain the posteriori distribution, we invoke a Monte Carlo-Metropolis method (e.g., Johnson and Segall, 2004). We apply box functions for the a priori distributions of V_1, V_2, and alpha. This means that the distributions are constant within the bounds and zero outside the bounds. We start a random walk in the model space from which the priori distribution is sampled. The probability of visiting the model $\mathbf{m}_j$ only depends on the current model $\mathbf{m}_i$, which is generated randomly from $\mathbf{m}_i$ with d unknowns:

$$\mathbf{m}_j = \mathbf{m}_i + \sum_{k=1}^{d} \alpha_k \gamma_k \mathbf{e}_k, \quad (5)$$

in which α_k represents the step size, γ_k represents a uniform random deviation from −1 to 1, and $\mathbf{e}_k$ denotes the unit vector along the kth axis in the parameter space. The random walk steps to the next model with probability (the Metropolis acceptance probability):

$$P_{ij} = \min\left(1, \frac{\rho_D(g(\mathbf{m}_j))}{\rho_D(g(\mathbf{m}_i))}\right), \quad (6)$$

which equals 1 for $\rho_D(g(\mathbf{m}_j)) \geq \rho_D(g(\mathbf{m}_i))$ and is $\frac{\rho_D(g(\mathbf{m}_j))}{\rho_D(g(\mathbf{m}_i))}$ when $\rho_D(g(\mathbf{m}_j)) < \rho_D(g(\mathbf{m}_i))$. The acceptance efficiency is defined as the sum of acceptance probabilities for all transitions.

Data preparation and model setup. We construct one profile of GPS velocities across the KMPJF and TLS of the EKLF from the works of Diao *et al.* (2019) and Wang and Shen (2020), revealing the far-fault and near-fault interseismic crustal motions of northeastern Tibet (Fig. S1, available in the supplemental material to this article). A total of 36 GPS stations with high signal-to-noise ratios (SNRs) are selected in this study. Given that the depth extent of the coseismic rupture of the 2001 M_w 7.8 Kokoxili earthquake is up to 20 km (Zhao *et al.*, 2021), we set the thickness of the elastic plate (locking depth) as 20 km for the KMPJF and TLS ($H1$ = $H2$ = 20 km), the same as the assumptions of Diao *et al.* (2019) and Zhu *et al.* (2021). The detailed tests of the locking depth will be discussed subsequently. During the inversion, the parameter space is placed within wide priori bounds: $0 < V_1(\mathrm{mm/yr}) < 10, 0 < V_2(\mathrm{mm/yr}) < 20, 0 < \mathrm{alpha(mm/yr)} < 20$. Finally, our MCMC inversion runs over 500,000 iterations and produces the acceptance rate of ~53% of the posterior distribution from which we estimate both the maximum a posteriori probability solution and marginalized probability distributions for each parameter.

Static finite-fault inversion based on geodetic data

GPS data processing. The GPS position time series at daily intervals are from the Crustal Movement Observation Network of China (CMONOC), which are processed using the programs GAMIT and GLOBK (e.g., Herring *et al.*, 2015). During the process, the ionospheric effects are eliminated by the ionosphere-free linear combinations; the tropospheric refractivity is modeled using the Global Mapping function; the ocean tidal correction is performed by the FES2004 model (e.g., Boehm *et al.*, 2006; Zheng *et al.*, 2017). In addition, the absolute antenna phase calibration is available in the International GNSS Service (IGS) antenna calibration file (e.g., Dach *et al.*, 2015). The CMONOC utilizes the IGS final products and combines these loosely constrained daily solutions with global solutions (Yu *et al.*, 2019). The least-squares fitting method is adopted to model the GPS time series and estimate parameters for each component (east, north, and up) of every station (Text S1).

A total of 12 available GPS observations that captured the coseismic deformation of the Maduo earthquake with high SNRs are selected (Fig. S2). Given the large uncertainties of 6–12 mm for the vertical components, only horizontal GPS displacements are used in the inversion (Table S1). The largest displacement is observed at the GPS station QHMD, located ~39 km north of the epicenter, with an ~26 cm horizontal displacement (Fig. S2).

InSAR data processing. The Interferometric Synthetic Aperture Radar (InSAR) observations have been proven effective in imaging the ground deformation associated with destructive earthquakes and are especially sensitive to the near-east–west deformation. For the 2021 Maduo earthquake, we use Sentinel-1A/B terrain observations acquired in Progressive mode from the European Space Agency to obtain the coseismic surface deformation (see Data and Resources). The reference images for both ascending and descending tracks were acquired on 20 May 2021, and 26 May 2021, covering the Maduo event. All of the images are processed using the GAMMA software based on the conventional two-pass differential InSAR method with multilook factors of 2 and 10 in the azimuth and range directions, respectively (e.g., Werner *et al.*, 2001). To remove the topographic phase, we use a Shuttle Radar Topography Mission-30 digital elevation model during interferogram formation. We filter and unwrap the interferograms by the power spectrum method and minimum cost flow algorithm (Goldstein and Werner, 1998; Werner *et al.*, 2001). Moreover, the regular stripes caused by orbital or ionospheric

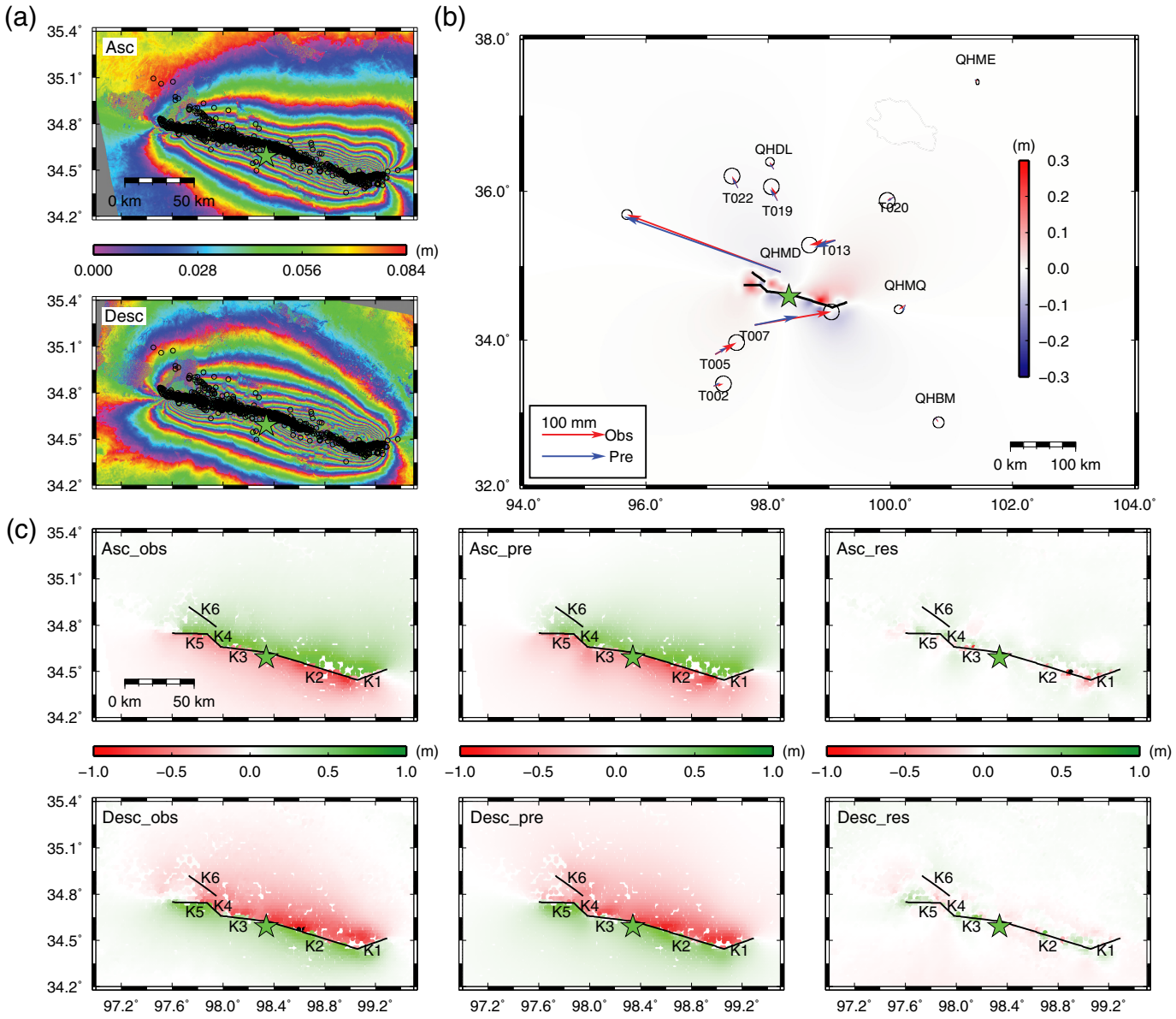

effects are removed from the interferograms by fitting a linear polynomial using data outside the deformation region.

Figure 2 shows the ascending and descending interferograms, revealing that the Synthetic Aperture Radar (SAR) data captured the coseismic deformation associated with the Maduo earthquake well. A significant line of sight displacement jump can be observed due to the fault movements in opposite directions, perfectly defining the surface fault traces of the Maduo event (Fig. 2c). The ascending interferogram shows a deformation pattern with a peak uplift of ~0.97 m to the north and a peak subsidence of ~0.85 m to the south. However, the descending interferogram demonstrates a diametrically opposite displacement field to the ascending interferogram, revealing a deformation pattern with a peak uplift of ~0.94 m on the south and peak subsidence of ~1.09 m on the north. Such phenomena indicate that the Maduo earthquake is dominated by strike-slip components

Figure 2. Maps of geodetic observations and predictions. (a) Observed ascending and descending interferograms. (b) Comparison of GPS observations and model predictions. Red and blue arrows indicate the observed and predicted horizontal GPS displacements, respectively. The background is the modeled vertical surface deformation assuming uniform isotropic elastic half-space with the rigidity of 30 GPa. (c) Comparison of the line of sight displacements between observations and predictions. The first and second columns represent the observed and predicted Interferometric Synthetic Aperture Radar (InSAR) displacements, respectively, and the third column indicates their residuals. The black lines are the fault surface traces of the 2021 Maduo earthquake. The green star is the epicenter of the Maduo event. Black circles denote the relocated aftershocks from Wang, Fang, *et al.* (2021). The color version of this figure is available only in the electronic edition.

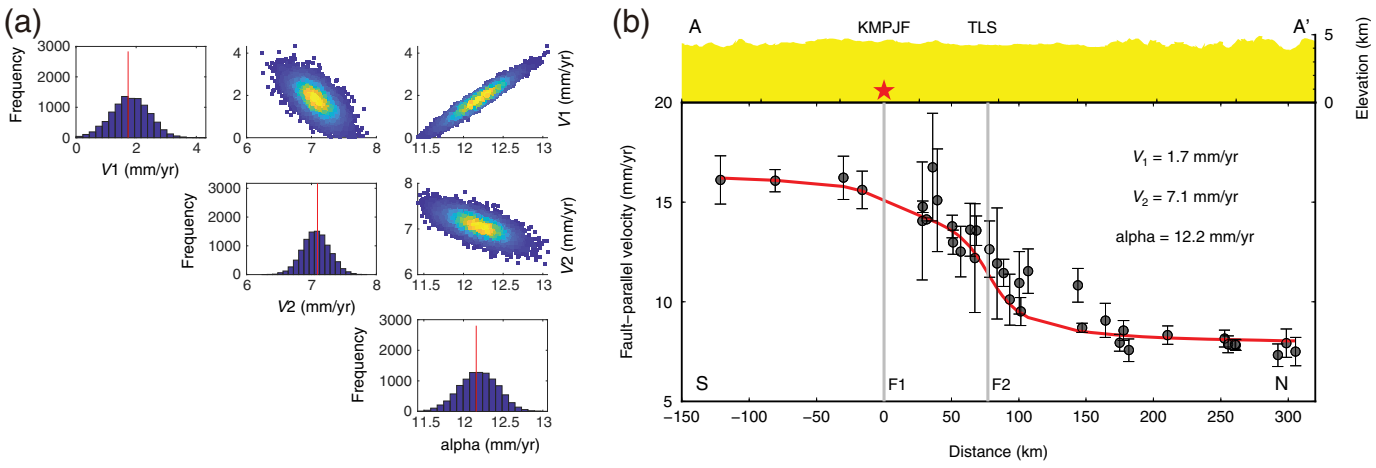

Figure 3. Probability distribution of parameters and data fitting. (a) Estimating fault parameters for the KMPJF and Tuosuo Lake segment (TLS) of the EKLF from our optimal dislocation model. Locking depth is set at 20 km. Red lines denote our maximum a posteriori probability solutions. Scatter dots indicate the occurrence frequency, in which cold colors denote low frequency and warm colors denote high frequency. (b) GPS data fitting. The red curve represents the fault-parallel velocity predictions based on our preferred model. The fault-parallel ground movements indicate high-strain rates in the TLS zone, but low ones across the KMPJF. Error bars represent 95% confidence. The red star represents the 2021 Maduo earthquake. F1 and F2 denote the KMPJF and TLS of the EKLF, respectively. The color version of this figure is available only in the electronic edition.

(Ji *et al.*, 2017), consistent with the reported nodal plain solutions of the mainshock.

Model parameters and inversion strategy. We set all fault planes to extend to the Earth's surface based on the observed ground rupture (Li *et al.*, 2021). The refined surface traces of seismogenic faults have been well mapped by the amplitude pixel offsets of SAR image pairs, which are further smoothed to shape the top edges of our preferred fault model, separating the main fault plane of the KMPJF into five subsegments (K1–K5). Their strikes are ∼250°, ∼287°, ∼276°, ∼313°, and ∼271° from K1 to K5, respectively. The fault surface trace of the secondary fault branch (K6) with a strike of ∼306° and dip angles of all fault subsegments are determined by additional a priori information on fault geometry from the relocated aftershock distribution (Fig. 2 and Fig. S3, Wang, Fang, *et al.*, 2021). Wang, Fang, *et al.* (2021) first selected the seismic group using a ± 5 km square window and then obtained the corresponding dip angles by linearly fitting the deviation distances and depths of the relocated aftershocks, clearly demonstrating the variation of the dip angles along strike. The KMPJF dips to the northwest with a high angle of 91° at the southeast end (K1); then the fault strike rotates clockwise by ∼37°, and the fault plane is still almost vertical along strike (88°) but dips to the northeast (K2). On the fault subsegment K3, the dip angle jumps to 80° (dip to northeast). Then, the K4 fault plane dips to southwest at a dip angle of 87° (93°, dip to northeast) into the fault segment K4 and becomes shallower at the northwest end of the rupture (K5, 83°, dip to southwest). For the subsegment K6, it dips to the northeast at an angle of 86° (Wang, Fang, *et al.*, 2021). All dip angles are assumed constant down-dip. During the inversion, all fault planes are discretized into rectangular meshes of ∼2.0 × 2.0 km in size, and the KMPJF and the secondary fault branch involve 984 and 144 patches, respectively.

We first assume a uniform slip distribution over a rectangular fault plane and compute Green's functions of plane dislocations by integrating point-source Green's functions over the fault plane. Then, the downsampled InSAR data and GPS coseismic observations are used to jointly invert the coseismic slip on the fault planes. We apply the steepest descent method to address this problem: one of the gradient methods (e.g., Wang *et al.*, 2009; Guo *et al.*, 2019; Tang *et al.*, 2021). For a more stable inversion, two constraints are applied: one is that the peak slip cannot be greater than 15 m, and the other is that the rake angle of each subfault is allowed to vary from −90° to 90°. The objective function is defined by

$$F(\mathbf{m}) = \|\mathbf{Gm} - \mathbf{y}\|^2 + \alpha^2\|\mathbf{L\tau}\|^2, \quad (7)$$

in which $\mathbf{G}$ represents Green's function; $\mathbf{m}$ is the slip vector, including the strike-slip and dip-slip components; and $\mathbf{y}$ indicates the GPS and InSAR data. α^2 represents the positive smoothing factor, which is set as 0.07 based on the trade-off curve between model roughness and data misfit (Fig. S4). $\mathbf{L}$ denotes the finite-difference approximation of the Laplacian operator, and $\boldsymbol{\tau}$ represents the shear stress drop linearly related to the slip distribution.

Results and Discussion

Kinematic fault-slip rates

Figure 3a demonstrates a posteriori PDF for estimated parameters on profile A–A′. Results show that the slip rate of the

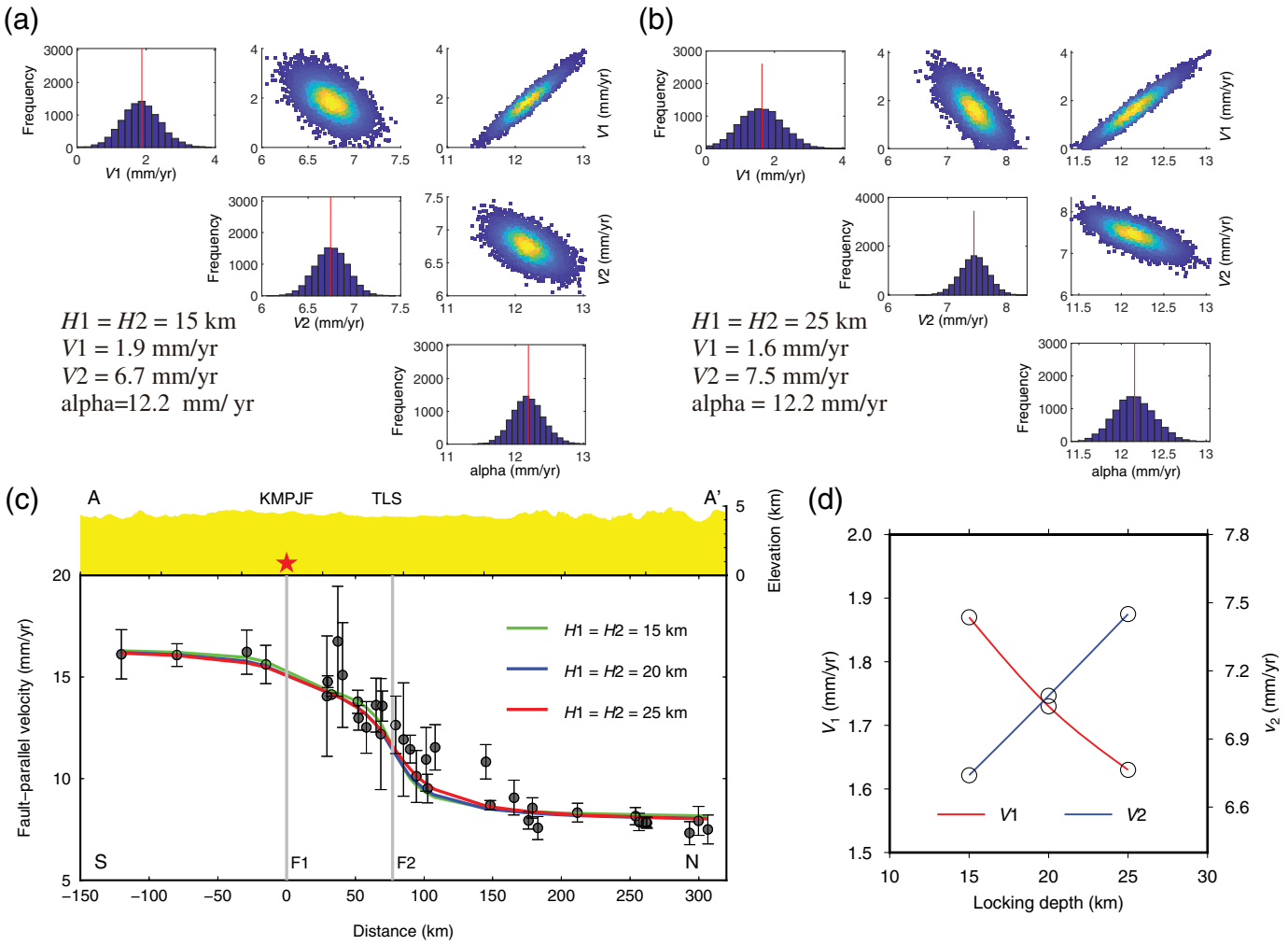

KMPJF is resolved with a maximum a posteriori probability solution (MAPS) of 1.7 mm/yr, ranging from 0.9 to 2.5 mm/yr (95% confidence interval), consistent with the reference of less than 3 mm/yr from Wang *et al.* (2013). For the TLS of the EKLF, the slip rate is quite well constrained in the range of 6.8–7.4 mm/yr (95% confidence interval) with a MAPS of 7.1 mm/yr (Fig. 3a), which is in the middle of 6.5–11.5 mm/yr for the geological slip rates (Van der Woerd *et al.*, 2002; Guo *et al.*, 2007) and is larger than the geodetic slip rate of 5.5 ± 0.7 mm/yr based on a viscoelastic earthquake cycle model (Diao *et al.*, 2019). The near-field GPS data on both sides of the KMPJF are relatively sparse, so the uncertainty of the slip rate of the KMPJF is larger than that of the TLS. In addition, our results are slightly larger than those of Zhu *et al.* (2021) (KMPFJ: 1.2 ± 0.8 mm/yr; TLS: 5.4 ± 0.3 mm/yr), which may be attributed to the different data set, inversion method, and dislocation model. As shown in Figure 3a, the alpha is also well constrained in a narrow range of 11.9–12.6 mm/yr with a MAPS of 12.2 mm/yr. Figure 3b shows the results of the parameters inversion, revealing that most surface deformation can be satisfactorily recovered.

To simplify the model, we fix the same locking depth for the KMPJF and TLS ($H1 = H2$) based on previous studies in our elastic dislocation model (e.g., Diao *et al.*, 2019; Zhao *et al.*, 2021; Zhu *et al.*, 2021). To testify the robustness of the assumption, we further perform the sensitivity tests of the observations to different locking depths. As shown in Figure 4, we test the locking depths of 15 and 25 km with other parameters kept constant, respectively, and find that the simulation results only slightly change. Therefore, the GPS observations are not sensitive to the locking depth or to the locking depths of the KMPJF and TLS being different (Fig. S5), so our assumption of fixing the locking depth is reasonable. In addition, we find that when $H1$ equals $H2$, the TLS would make a greater contribution to the surface deformation as the locking depth increases

Figure 4. Sensitivity tests of the observed GPS data to different locking depths. Estimating fault parameters for the KMPJF and TLS based on the locking depth of (a) 15 and (b) 25 km. When the locking depth is 15 km, the optimal fault-slip rates V_1 and V_2 are 1.9 and 6.7 mm/yr, respectively. When the locking depth is 25 km, the optimal fault-slip rates V_1 and V_2 are 1.6 and 7.5 mm/yr, respectively. (c) GPS data fitting based on different locking depths. (d) Variation of fault-slip rates with the locking depth. Other symbols are the same as Figure 3. The color version of this figure is available only in the electronic edition.

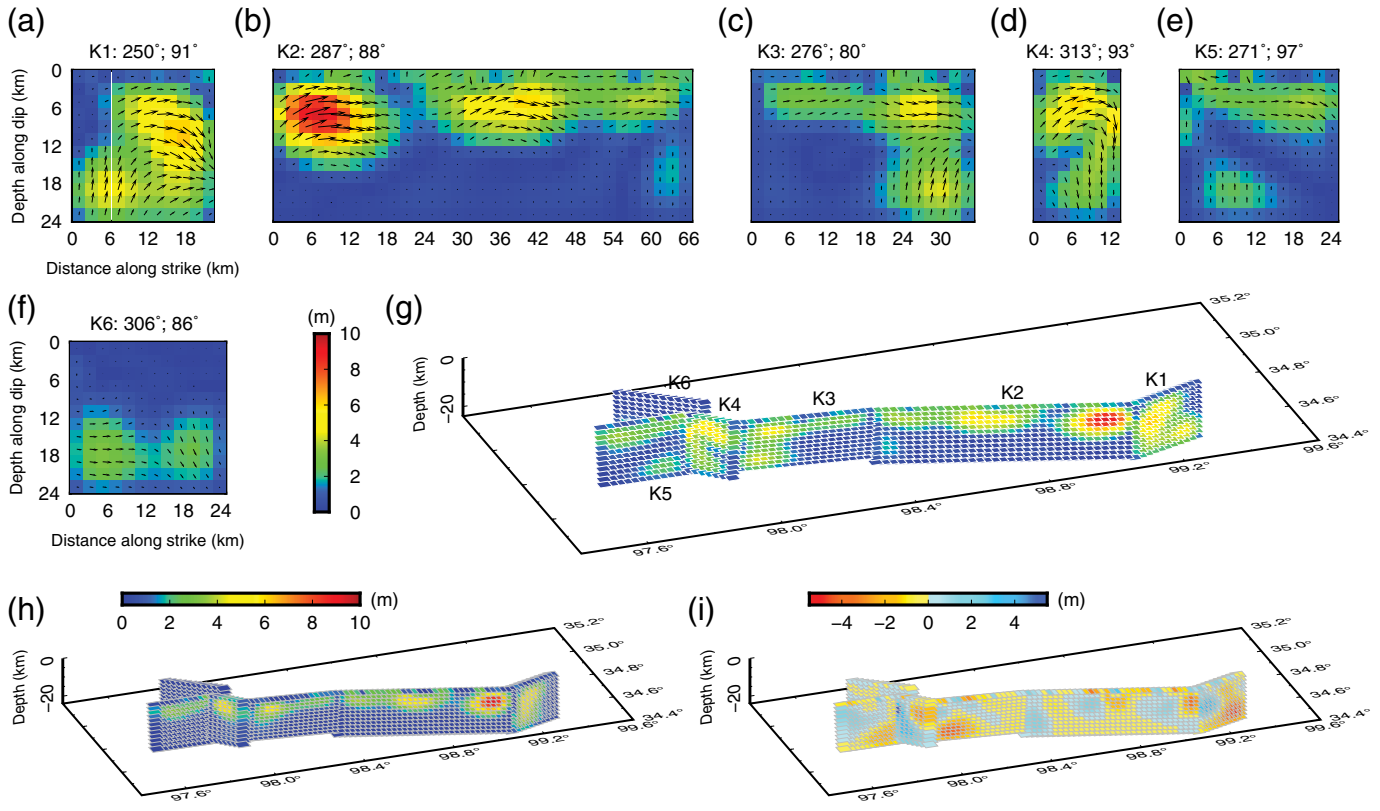

Figure 5. Our preferred rupture model of the 2021 Maduo earthquake. (a–f) The coseismic slip distribution along dip for different fault subsegments. K1–K5 and K6 are the fault subsegments on the KMPJF and the second branch fault, respectively. (g) The 3D fault geometry and slip distribution. (h) Sinistral and (i) thrust or normal slip amplitudes. The color version of this figure is available only in the electronic edition.

(Fig. 4); when $H1$ is different from $H2$, the fault-slip rate would become larger with increasing the locking depth (Fig. S5).

However, there are two shortcomings in our model. One is that our model is constructed based on the elastic dislocation theory, ignoring the effects of viscoelastic relaxation. Because deriving an analytical solution of multiple faults based on the viscoelastic earthquake-cycle model is difficult, it may be feasible to simply sum the earthquake-cycle deformation from the two faults with their respective parameters based on a linear Maxwell rheology. We would not be getting into stress interactions between two faults or corresponding effects on earthquake recurrence intervals or be worried about stress and time-dependent viscosity of power-law rheologies. It is worth further study to confirm whether it is actually okay to simply superimpose the solutions. Similarly, one could do that with the equivalent time-dependent elastic dislocation solution that is a fully linear problem (e.g., Savage, 1990; Lisowski *et al.*, 1991). Moreover, the numerical (finite element) version with dimensions may be a good solution. Another disadvantage is that we only consider the effects of the KMPJF and TLS of the EKLF, ignoring the contributions from other fault branches, and it would lead to a slight overestimation of the fault-slip rates (Zhu *et al.*, 2021). Because the GPS data on the south side are relatively sparse, it is not enough to distinguish the effects of more fault branches.

Geometric irregularities and coseismic slip pattern

The coseismic geodetic observations and model predictions are demonstrated in Figure 2, displaying a satisfactory fitting pattern. The optimal slip distribution, shown in Figure 5, has a released seismic moment of about 1.5×10^{20} N · m, equivalent to an M_w 7.39 event, within the range of seismic moments from the USGS (1.3×10^{20} N · m) and Global CMT (1.7×10^{20} N · m) catalogs. We estimate an equivalent moment tensor based on our preferred slip model using a tensorial sum of moment tensors of all dislocation patches. As shown in Figure 1c, the respective focal mechanism is denoted as a black focal mechanism plot, similar to the Global CMT solution. The average stress drops for the six fault subsegments are 6.1, 4.7, 4.0, 7.5, 3.1, and 5.1 MPa, respectively, consistent with the stress drop of 6.0 ± 1.0 MPa for global intraplate earthquakes (e.g., Allmann and Shearer, 2009). Our model reveals that most fault-slip concentrates in the shallow crust, especially on the fault subsegments K2 and K3, and the high-slip patches correspond mostly to the straight and continuous structures of the KMPJF (Fig. 5). The slip distribution on the fault subsegments K1 and K4 has comparable amplitudes, with significant thrust and normal components (Fig. 5a,d,i). The slip distribution on the subsegment K2 is divided into two high-slip zones by a

~6 km slip gap. Both are dominated by the sinistral slip, and the strike-slip components are located near the surface (Fig. 5h). The eastern one is concentrated at 0–12 km depth, with the maximum slip of ~9.3 m; another one occurs at a length of ~60 km along strike and shallower depth (Fig. 5b). A minor peak is found on the subsegments K3 and K5, where the average slips reach ~1.7 and ~1.4 m, respectively. In addition, two obvious geometrical irregularities are related to low-slip zones (<2 m). Overall, the mean coseismic slip (S) on the main fault KMPJF is ~2.13 m. Combining the slip rate of 1.7 ± 0.8 mm/yr obtained earlier, we can estimate the earthquake interval (T) based on the following equation (Shen *et al.*, 2009):

$$T = \frac{S}{v}. \tag{8}$$

Therefore, we propose that the recurrence period is about 1250^{+1120}_{-400} yr.

Most aftershocks on the KMPJF are found to cluster characteristically at 8–13 km depth, revealing a complementary pattern with the coseismic high-slip regions (Fig. S3, Wang, Fang, *et al.*, 2021). The dense aftershock populations are located near the intersections of faults segments, which may be triggered by the surrounding large coseismic slip. Few aftershocks (Wang, Fang, *et al.*, 2021) and negligible background seismicity (Wen *et al.*, 2011) in the middle subsegment K2 might suggest a ≥20 km seismicity gap along strike (Fig. S3; Wang, Fang, *et al.*, 2021). Below the depth of ~10 km, the region is also characterized by a small amount of slip. In addition, the aftershock density is low along the fault subsegment K4, in contrast to the widely distributed slip from the ground surface down to ~20 km depth. It reveals that most accumulated strain energy is released by the coseismic slip. Notably, uncertainties of deep slip are greater because the geodetic observations are less sensitive to slip at depth.

Our results also demonstrate a small amount of slip on the second branch fault extending northeastward, with a maximum slip of ~3.2 m and an average slip of ~1.1 m (Fig. 5f). Model inversions without this branch fault lead to a significantly worsened fit to the GPS data (Fig. S6). Lack of surface rupture on this fault subsegment K6 and aftershocks at depths of 10–25 km (Fig. S3; Wang, Fang, *et al.*, 2021) indicate that a strong shallow barrier survived the Maduo coseismic failure (Wang *et al.*, 2011). The surrounding historical earthquakes may have produced a stress shadow on this subsegment, thus hindering the slip through the barrier.

As shown in Figure 5, such complex slip behavior may be attributed to the structural complexities, which play a primary role in controlling rupture propagation (e.g., Yang *et al.*, 2013; Chen and Yang, 2020). Geometrical complexity could lead to variations in preseismic loading, which has a significant impact on the dynamic interaction of faults (e.g., Duan and Oglesby, 2006). The slip on the next asperity may be triggered dynamically, rather than representing a single passing through the fracture front (Wang *et al.*, 2011), as evidenced in dynamic rupture simulations (e.g., Yao and Yang, 2020).

In addition, we simulate the vertical deformation based on the PSGRN/PSCMP software (Wang *et al.*, 2006), which can determine the surface deformation due to the common geophysical sources. The driving source is our preferred slip model assuming a rigidity of 30 GPa. Results show that uplift is concentrated near the subsegment K5 and in the northeast of K2 and K3, and other regions are mainly manifested as subsidence (Fig. 2b).

Tectonic implications and future seismic hazards

Tectonic implications. Interseismic locking distribution has been widely used to evaluate the future seismic potential, especially in subduction zones (e.g., Jiang *et al.*, 2015; Hsu *et al.*, 2016). Based on locking distribution, coseismic rupture scenarios have also been derived to further quantitatively assess the seismic hazard (Yang, Yao, He, and Newman, 2019; Yang *et al.*, 2019). However, the distribution of continental faults is relatively complex, and there are often multiple faults at the edge of blocks, jointly participating in the allocation and accumulation of tectonic strains. As shown in Figure S1, the secular patterns of strain accumulation and surface deformation shown by GPS before the 2021 Maduo earthquake are striking. There is a marked contrast between the deformation rates occurring in the northern TLS of the EKLF compared with the KMPJF. The northern TLS deformed at a rate of about 7.1 mm/yr, whereas the neighboring Kunlun Mountain Pass–Jiangcuo fault zone, in which the 2021 earthquake took place, was only subject to minor deformation of ~1.7 mm/yr. It, therefore, seemed reasonable to expect that large earthquakes are more likely to occur in the rapidly deforming parts of northern EKLF, rather than the narrow slowly deforming KMPJF zone. It is undeniable that the Maduo earthquake stands out as unusual in recorded history, being another event occurring in a slowly deforming region after the 2008 M_w 7.9 Wenchuan earthquake (Zhang, 2013).

Previous scientific knowledge of surface deformation and fault kinematics leads us to maintain an optimistic sense of security about seismic hazards in regions with low-slip rates. The interseismic geodetic measurements can only constrain the short-term deformation rate, but they cannot reflect the stored strain energy that will propel the next earthquake. Wang, Zhu, *et al.* (2021) argued that, if the seismic recurrence time is long or the viscosity of viscoelastic substrate is low, most energy for the next major earthquake is accumulated during the early time of the earthquake cycle, and deformation rates gradually decay to a minimum in the later stage of the interseismic period. Thus, in some situations, the observed low-fault deformation rates do not imply a low-seismic potential but rather indicate a higher likelihood of a major earthquake. We must now review previous charts of seismic risk,

and identify other potential sources of hazard (Zhang, 2013) by jointly interpreting geodetic data in the viscoelastic framework with paleoseismic and historical constraints (Wang, Zhu, *et al.*, 2021).

Seismic hazards assessment. In recent years, Coulomb failure stress change (ΔCFS) has been widely used for probing the migration of seismicity over time (e.g., Nalbant *et al.*, 1998), the characteristics of aftershock distribution (e.g., Guo *et al.*, 2019), and the interaction and triggering among major earthquakes (e.g., Segou and Parsons, 2018); it has become one the most effective ways to investigate future seismic hazards. It is calculated based on the expression:

$$\Delta\mathrm{CFS} = \Delta\tau + \mu'\Delta\sigma_n, \tag{9}$$

in which $\Delta\tau$ and $\Delta\sigma_n$ represent the changes of the shear and normal stresses, respectively. μ' is the effective frictional coefficient. From this equation, the positive ΔCFS could increase the tectonic loading on faults and push them closer to failure. In contrast, the negative ΔCFS would delay the occurrence of seismicity, resulting in the postseismic quiescence (e.g., Shan *et al.*, 2015; Pope and Mooney, 2020).

In this article, we calculate the ΔCFS caused by the 2021 Maduo earthquake using the program PSGRN/PSCMP (Wang *et al.*, 2006). Usually, the effective frictional coefficient μ' is assumed to be 0.2–0.4 for high-angle strike-slip faults, and a different μ' has little effect on the ΔCFS pattern (e.g., Parsons *et al.*, 1999; Xiong *et al.*, 2010; Shan *et al.*, 2013, 2015; Guo *et al.*, 2020). Therefore, 0.4 is assigned for the numerical simulation, consistent with the model of Shan *et al.* (2015). The main seismogenic fault KMPJF with a simplified fault geometry (strike: 285°; dip: 90°) is set as our receiver fault, and our preferred slip model is the driving source. Because most aftershocks are concentrated within the range of 8–13 km, we calculate Green's function at a depth of 10.5 km. Results show that most aftershocks occurred in areas with positive stress changes, but there were a large number of aftershocks located in the stress shadow, which may be related to the background tectonic stress (e.g., Tang *et al.*, 2021). As shown in Figure 6a, the positive ΔCFS is mainly concentrated on both flanks of the source region, implying a high-seismic hazard. Shan *et al.* (2015) argued that the historical earthquakes from 1879 to 2008 significantly increased the stress on the MMS of the EKLF, bringing the MMS closer to failure for ∼160 and ∼250 yr, respectively. The MMS is a large seismic gap with little seismicity, in which the recurrence intervals of the MMS are 500–700 yr and ∼1000 yr, respectively (Li, Zu, *et al.*, 2011; Shan *et al.*, 2015). In addition, the last large earthquakes in these two segments occurred 514–534 and 1055–1524 yr ago, respectively (Li, Zu, *et al.*, 2011). We thus further use the MMS as the receiver fault to estimate the ΔCFS caused by the 2021 Maduo earthquake (Fig. 6c). It is observed that the Maduo event imposes positive stress on the MMS, which can accelerate the occurrence of the next event in the Maqin–Maqu seismic gap. Therefore, it is very likely that a major earthquake will occur on the MMS in the near future.

In addition, to test whether the aftershocks near the secondary fault are induced by the slip on the main fault, we take the secondary fault as the receiver fault (strike: 306°; dip: 86°) and use the slip on the main fault as the driving source to calculate the ΔCFS on this secondary fault. Given that the aftershocks are concentrated within the range of 10–25 km, our simulation is performed assuming a focal depth of 18 km. Results show that the negative ΔCFS caused by the slip on the main fault hinders the seismicity on the fault subsegment K6 (Fig. 6b). This also proves from the side that this secondary fault participates in the contribution of coseismic deformation.

Conclusions

Based on the interseismic GPS velocities, we derive that the slip rates of the KMPJF and TLS of the EKLF are 1.7 ± 0.8 and 7.1 ± 0.3 mm/yr, respectively. In addition, we apply GPS and InSAR data to untie the complex fault geometry and detailed coseismic slip distribution of the 2021 Maduo earthquake. Our preferred model shows that high slips are concentrated in the shallow crust, accommodated by six steeply dipping fault subsegments, with a peak slip of ∼9.3 m at 7 km depth. The estimated seismic moment is about 1.5×10^{20} N · m, equivalent to an M_w 7.39 event. The occurrence of the 2021 Maduo earthquake once again verifies the enlightenment that the 2008 Wenchuan earthquake gave us. The slowly slipping faults may also have a high-seismic potential. It is necessary for us to reevaluate the previous earthquake hazard maps, especially for areas where the deformation rate is low and no earthquake has occurred for a long time. Moreover, given that the background tectonics and earthquake-induced stress increment, MMS may be in the late earthquake cycle and have a high-seismic potential, which deserves our great attention.

Data and Resources

All data in this article are available. The Synthetic Aperture Radar (SAR) images are obtained from European Space Agency available at https://search.asf.alaska.edu/#/. The coseismic Global Positioning System (GPS) displacements used in this work are listed in Table S1. The focal mechanisms of the Maduo earthquake from the China Earthquake Networks Center (CENC), U.S. Geological Survey (USGS), Global Centroid Moment Tensor (Global CMT), and GeoForschungsZentrum (GFZ) are available at https://news.ceic.ac.cn/, https://earthquake.usgs.gov/, https://www.globalcmt.org/, and https://geofon.gfz-potsdam.de/, respectively. All websites were last accessed in October 2021. The supplemental material involves one text, six figures, and one table to support the discussion in the main article.

Declaration of Competing Interests

The authors acknowledge that there are no conflicts of interest recorded.

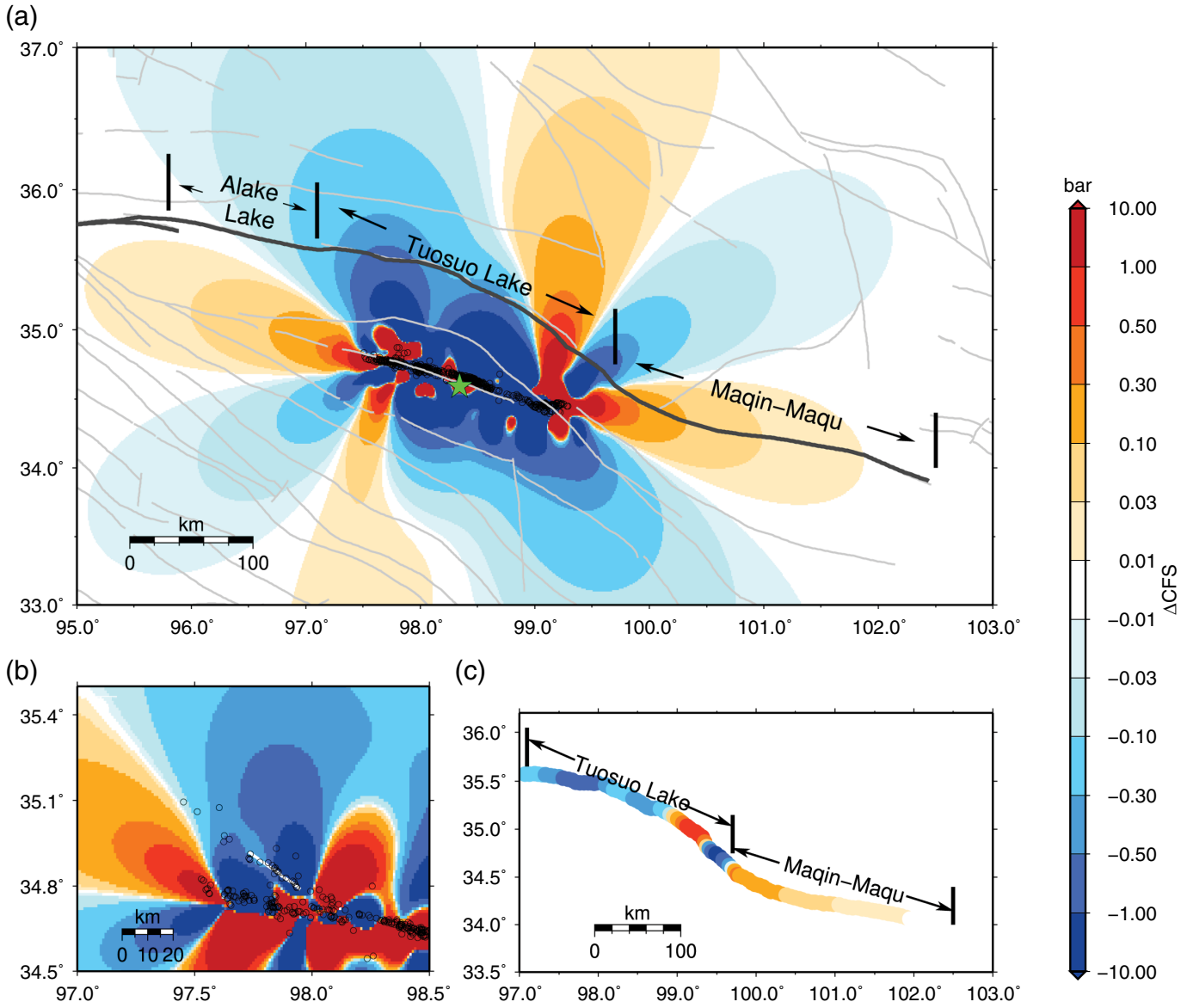

Figure 6. Coulomb failure stress change (ΔCFS) due to the 2021 Maduo earthquake. (a) ΔCFS caused by the Maduo earthquake at the depth of 10.5 km. Black dots are the aftershocks within the range of 8–13 km. The green star represents the epicenter of the Maduo event. (b) ΔCFS caused by the slip on the main fault KLMJF at the depth of 18 km. Black dots represent aftershocks with the depth greater than 10 km. The white line denotes the receiver fault (strike: 306° and dip: 86°). (c) ΔCFS along the TLS and Maqin–Maqu segments of the EKLF. The color version of this figure is available only in the electronic edition.

Acknowledgments

The authors thank the Editor Allison Bent, Zhe Jia, and one anonymous reviewer for comments that improved this article. The authors thank Kelin Wang from Geological Survey of Canada and Roland Bürgmann from UC Berkeley for discussion and suggestions and Han Chen for help in Interferometric Synthetic Aperture Radar (InSAR) data processing from State Key Laboratory of Earthquake Dynamics, Institute of Geology, China Earthquake Administration. This study is supported by the National Key R&D Program of China (2018YFC1503400), China Earthquake Science Experiment Project (CEA) (Grant Number 2018CSES0102), Hong Kong Research Grant Council (Grant Numbers 14306119 and 14306418), CUHK Direct Grant from Faculty of Science, Beijing Natural Science Foundation (8204077), and National Natural Science Foundation of China (42004010).

References

Allmann, B. P., and P. M. Shearer (2009). Global variations of stress drop for moderate to large earthquakes, *J. Geophys. Res.* **114,** doi: 10.1029/2008JB005821.

Aslan, G., C. Lasserre, Z. Cakir, S. Ergintav, S. Özarpaci, U. Dogan, R. Bilham, and F. Renard (2019). Shallow creep along the 1999 Izmit earthquake rupture (Turkey) from GPS and high temporal resolution interferometric synthetic aperture radar data (2011–2017), *J. Geophys. Res.* **124,** 2218–2236, doi: 10.1029/2018JB017022.

Boehm, J., A. Niell, P. Tregoning, and H. Schuh (2006). Global mapping function (GMF): A new empirical mapping function based

on numerical weather model data, *Geophys. Res. Lett.* **33,** doi: 10.1029/2005GL025546.

Chen, X., and H. Yang (2020). Effects of seismogenic width and low-velocity zones on estimating slip-weakening distance from near-fault ground deformation, *Geophys. J. Int.* doi: 10.1093/gji/ggaa385.

Dach, R., S. Lutz, P. Walser, and P. Fridez (2015). *Bernese GNSS Software Version 5.2*, University of Bern, Bern Open Publishing, Bern, Switzerland.

Diao, F., X. Xiong, R. Wang, T. R. Walter, Y. Wang, and K. Wang (2019). Slip rate variation along the kunlun fault (Tibet): Results from new GPS observations and a viscoelastic earthquake-cycle deformation model, *Geophys. Res. Lett.* **46,** 2524–2533, doi: 10.1029/2019GL081940.

Duan, B., and D. D. Oglesby (2006). Heterogeneous fault stresses from previous earthquakes and the effect on dynamics of parallel strike-slip faults, *J. Geophys. Res.* **111,** doi: 10.1029/2005JB004138.

England, P., and G. Houseman (1986). Finite strain calculations of continental deformation: 2. Comparison with the India-Asia Collision Zone, *J. Geophys. Res.* **91,** 3664–3676, doi: 10.1029/JB091iB03p03664.

Furuya, M., and T. Yasuda (2011). The 2008 Yutian normal faulting earthquake (Mw 7.1), NW Tibet: Non-planar fault modeling and implications for the Karakax fault, *Tectonophysics* **511,** 125–133, doi: 10.1016/j.tecto.2011.09.003.

Goldstein, R. M., and C. L. Werner (1998). Radar interferogram filtering for geophysical applications, *Geophys. Res. Lett.* **25,** 4035–4038, doi: 10.1029/1998GL900033.

Guo, J., A. Lin, G. Sun, and J. Zheng (2007). Surface ruptures associated with the 1937 M 7.5 Tuosuo Lake and the 1963 M 7.0 Alake Lake earthquakes and the paleoseismicity along the Tuosuo Lake segment of the Kunlun Fault, Northern Tibet, *Bull. Seismol. Soc. Am.* **97,** 474–496, doi: 10.1785/0120050103.

Guo, R., Y. Zheng, W. Tian, J. Xu, and W. Zhang (2018). Locking status and earthquake potential hazard along the middle-south Xianshuihe fault, *Remote Sens.* **10,** 2048, doi: 10.3390/rs10122048.

Guo, R., Y. Zheng, and J. Xu (2020). Stress modulation of the seismic gap between the 2008 Ms 8.0 Wenchuan earthquake and the 2013 Ms 7.0 Lushan earthquake and implications for seismic hazard, *Geophys. J. Int.* **221,** 2113–2125, doi: 10.1093/gji/ggaa143.

Guo, R., Y. Zheng, J. Xu, and Z. Jiang (2019). Seismic and aseismic fault slip associated with the 2017 Mw 8.2 Chiapas, Mexico, earthquake sequence, *Seismol. Res. Lett.* **90,** 1111–1120, doi: 10.1785/0220180262.

Herring, T. A., M. A. Floyd, R. W. King, and S. C. McClusky (2015). *Global Kalman Filter VLBI and GPS Analysis Program, GLOBK Reference Manual, Release 10.6*, Department of Earth, Atmospheric and Planetary Sciences, Massachusetts Institute of Technology, Cambridge, Massachusetts.

Hsu, Y.-J., S.-B. Yu, J. P. Loveless, T. Bacolcol, R. Solidum, A. Luis, A. Pelicano, and J. Woessner (2016). Interseismic deformation and moment deficit along the Manila subduction zone and the Philippine Fault system, *J. Geophys. Res.* **121,** 7639–7665, doi: 10.1002/2016JB013082.

Ji, L., C. Liu, J. Xu, L. Liu, F. Long, and Z. Zhang (2017). InSAR observation and inversion of the seismological fault for the 2017 Jiuzhaigou earthquake Ms 7.0 earthquake in China, *Chin. J. Geophys.* **60,** no. 10, 4069–4082, doi: 10.6038/cjg20171032 (in Chinese).

Jiang, G., X. Xu, G. Chen, Y. Liu, Y. Fukahata, H. Wang, G. Yu, X. Tan, and C. Xu (2015). Geodetic imaging of potential seismogenic asperities on the Xianshuihe-Anninghe-Zemuhe fault system, southwest China, with a new 3-D viscoelastic interseismic coupling model, *J. Geophys. Res.* **120,** 1855–1873, doi: 10.1002/2014JB011492.

Jiang, Z., M. Wang, Y. Wang, Y. Wu, S. Che, Z.-K. Shen, R. Bürgmann, J. Sun, Y. Yang, H. Liao, *et al.* (2014). GPS constrained coseismic source and slip distribution of the 2013 Mw6.6 Lushan, China, earthquake and its tectonic implications, *Geophys. Res. Lett.* **41,** 407–413, doi: 10.1002/2013GL058812.

Johnson, K. M., and P. Segall (2004). Viscoelastic earthquake cycle models with deep stress-driven creep along the San Andreas fault system, *J. Geophys. Res* **109,** doi: 10.1029/2004JB003096.

Li, C., X. Xu, X. Wen, R. Zheng, G. Chen, H. Yang, Y. An, and X. Gao (2011). Rupture segmentation and slip partitioning of the mid-eastern part of the Kunlun Fault, north Tibetan Plateau, *Sci. China Earth Sci.* **54,** 1730, doi: 10.1007/s11430-011-4239-5.

Li, H., J. Pan, A. Lin, Z. Sun, D. Liu, J. Zhang, C. Li, K. Liu, M. Chevalier, K. Yun, *et al.* (2016). Coseismic surface ruptures associated with the 2014 Mw 6.9 Yutian earthquake on the Altyn Tagh Fault, Tibetan Plateau, *Bull. Seismol. Soc. Am.* **106,** 595–608, doi: 10.1785/0120150136.

Li, Z., J. R. Elliott, W. Feng, J. A. Jackson, B. E. Parsons, and R. J. Walters (2011). The 2010 MW 6.8 Yushu (Qinghai, China) earthquake: Constraints provided by InSAR and body wave seismology, *J. Geophys. Res* **116,** doi: 10.1029/2011JB008358.

Li, Z., W. Li, T. Li, Y. Xu, P. Su, P. Guo, H. Sun, G. Ha, G. Chen, Z. Yuan, *et al.* (2021). Seismogenetic fault and coseismic surface deformation of the Maduo Ms 7.4 earthquake in Qinghai, China: A quick report, *Seismol. Geol.* **43,** 722–737.

Lisowski, M., J. C. Savage, and W. H. Prescott (1991). The velocity field along the San Andreas Fault in central and southern California, *J. Geophys. Res.* **96,** 8369–8389, doi: 10.1029/91JB00199.

Mosegaard, K., and A. Tarantola (2002). Probabilistic approach to inverse problems, in *The International Handbook of Earthquake and Engineering Seismology (Part A)*, H. K. L. William, H. Kanamori, P. C. Jennings, and C. Kisslinger (Editors), Elsevier, Amsterdam, The Netherlands, 237–265.

Nalbant, S. S., A. Hubert, and G. C. P. King (1998). Stress coupling between earthquakes in northwest Turkey and the north Aegean Sea, *J. Geophys. Res.* **103,** 24,469–24,486, doi: 10.1029/98JB01491.

Parsons, T., R. Stein, R. Simpson, and P. Reasenberg (1999). Stress sensitivity of fault seismicity: A comparison between limited-offset oblique and major strike-slip faults, *J. Geophys. Res.* **104,** no. B9, 20,183–20,202, doi: 10.1029/1999JB900056.

Pope, N., and W. D. Mooney (2020). Coulomb stress models for the 2019 Ridgecrest, California earthquake sequence, *Tectonophysics* **791,** 228555, doi: 10.1016/j.tecto.2020.228555.

Qiu, J., L. Ji, L. Liu, and C. Liu (2019). Seismogenic fault and tectonic significance of 1996 Karakoram Pass earthquake (Ms 7.1) based on InSAR, *Earth Planets Space* **71,** 108, doi: 10.1186/s40623-019-1089-4.

Ryder, I., R. Bürgmann, and F. Pollitz (2011). Lower crustal relaxation beneath the Tibetan Plateau and Qaidam Basin following the 2001 Kokoxili earthquake, *Geophys. J. Int.* **187,** 613–630, doi: 10.1111/j.1365-246X.2011.05179.x.

Savage, J. C. (1990). Equivalent strike-slip earthquake cycles in half-space and lithosphere-asthenosphere earth models, *J. Geophys. Res.* **95,** 4873–4879, doi: 10.1029/JB095iB04p04873.

Savage, J. C., and R. O. Burford (1973). Geodetic determination of relative plate motion in central California, *J. Geophys. Res.* **78,** 832–845, doi: 10.1029/JB078i005p00832.

Segou, M., and T. Parsons (2018). Testing earthquake links in Mexico from 1978 to the 2017 M = 8.1 Chiapas and M = 7.1 Puebla Shocks, *Geophys. Res. Lett.* **45,** 708–714, doi: 10.1002/2017GL076237.

Shan, B., X. Xiong, R. Wang, Y. Zheng, and R. B. S. Yadav (2015). Stress evolution and seismic hazard on the Maqin-Maqu segment of East Kunlun Fault zone from co-, post- and interseismic stress changes, *Geophys. J. Int.* **200,** 244–253, doi: 10.1093/gji/ggu395.

Shan, B., X. Xiong, R. Wang, Y. Zheng, and S. Yang (2013). Coulomb stress evolution along Xianshuihe–Xiaojiang Fault System since 1713 and its interaction with Wenchuan earthquake, May 12, 2008, *Earth Planet. Sci. Lett.* **377–378,** 199–210, doi: 10.1016/j.epsl.2013.06.044.

Shen, Z.-K., J. Sun, P. Zhang, Y. Wan, M. Wang, R. Bürgmann, Y. Zeng, W. Gan, H. Liao, and Q. Wang (2009). Slip maxima at fault junctions and rupturing of barriers during the 2008 Wenchuan earthquake, *Nature Geosci.* **2,** 718–724, doi: 10.1038/ngeo636.

Tang, X., R. Guo, J. Xu, H. Sun, X. Chen, and J. Zhou (2021). Probing the fault complexity of the 2017 Ms 7.0 Jiuzhaigou earthquake based on the InSAR data, *Remote Sens.* **13,** 1573, doi: 10.3390/rs13081573.

Van der Woerd, J., P. Tapponnier, F. J. Ryerson, A.-S. Meriaux, B. Meyer, Y. Gaudemer, R. C. Finkel, M. W. Caffee, Z. Guoguang, and X. Zhiqin (2002). Uniform postglacial slip-rate along the central 600 km of the Kunlun Fault (Tibet), from 26Al, 10Be, and 14C dating of riser offsets, and climatic origin of the regional morphology, *Geophys. J. Int.* **148,** 356–388, doi: 10.1046/j.1365-246x.2002.01556.x.

Wang, M., and Z.-K. Shen (2020). Present-day crustal deformation of continental china derived from GPS and its tectonic implications, *J. Geophys. Res.* **125,** e2019JB018774, doi: 10.1029/2019JB018774.

Wang, K., Y. Zhu, E. Nissen, and Z.-K. Shen (2021). On the relevance of geodetic deformation rates to earthquake potential, *Geophys. Res. Lett.* **48,** e2021GL093231, doi: 10.1029/2021GL093231.

Wang, L., R. Wang, F. Roth, B. Enescu, S. Hainzl, and S. Ergintav (2009). Afterslip and viscoelastic relaxation following the 1999 M 7.4 İzmit earthquake from GPS measurements, *Geophys. J. Int.* **178,** 1220–1237, doi: 10.1111/j.1365-246X.2009.04228.x.

Wang, Q., Q. Xuejun, L. Qigui, J. Freymueller, Y. Shaomin, X. Caijun, Y. Yonglin, Y. Xinzhao, T. Kai, and C. Gang (2011). Rupture of deep faults in the 2008 Wenchuan earthquake and uplift of the Longmen Shan, *Nature Geosci.* **4,** 634–640, doi: 10.1038/ngeo1210.

Wang, R., F. Lorenzo-Martín, and F. Roth (2006). PSGRN/PSCMP—A new code for calculating co- and post-seismic deformation, geoid and gravity changes based on the viscoelastic-gravitational dislocation theory, *Comput. Geosci.* **32,** 527–541, doi: 10.1016/j.cageo.2005.08.006.

Wang, W., L. Fang, J. Wu, H. Tu, L. Chen, G. Lai, and L. Zhang (2021). Aftershock sequence relocation of the 2021 MS7.4 Maduo earthquake, Qinghai, China, *Sci. China Earth Sci.* doi: 10.1007/s11430-021-9803-3.

Wang, Y., M. Wang, Z.-K. Shen, W. Ge, K. Wang, F. Wang, and J. Sun (2013). Inter-seismic deformation field of the Ganzi-Yushu fault before the 2010 Mw 6.9 Yushu earthquake, *Tectonophysics* **584,** 138–143, doi: 10.1016/j.tecto.2012.03.026.

Wen, Y.-Y., and K.-F. Ma (2010). Fault geometry and distribution of asperities of the 1997 Manyi, China (Mw = 7.5), earthquake: Integrated analysis from seismological and InSAR data, *Geophys. Res. Lett.* **37,** doi: 10.1029/2009GL041976.

Wen, X., G. Yi, and X. Xu (2007). Background and precursory seismicities along and surrounding the Kunlun fault before the Ms8.1, 2001, Kokoxili earthquake, China, *J. Asian Earth Sci.* **30,** 63–72, doi: 10.1016/j.jseaes.2006.07.008.

Wen, X., F. Du, P. Zhang, and F. Long (2011). Correlation of major earthquake sequences on the northern and eastern boundaries of the Bayan Har block, and its relation to the 2008 Wenchuan earthquake, *Chin. J. Geophys.* **54,** no. 3, 706–716, doi: 10.3969/j.issn.0001-5733.2011.03.010.

Werner, C., U. Wegmüller, T. Strozzi, and A. Wiesmann (2001). Gamma SAR and interferometric processing software, *Proc. of the ERS-ENVISAT Symposium*, Gothenburg, Sweden, 15–20 October 2000.

Xiong, X., B. Shan, Y. Zheng, and R. Wang (2010). Stress transfer and its implication for earthquake hazard on the Kunlun Fault, Tibet, *Tectonophysics* **482,** no. 1, 216–225, doi: 10.1016/j.tecto.2009.07.020.

Yang, H., Y. Liu, and J. Lin (2013). Geometrical effects of a subducted seamount on stopping megathrust ruptures, *Geophys. Res. Lett.* **40,** 1–6, doi: 10.1002/grl.50509.

Yang, H., S. Yao, B. He, and A. V. Newman (2019). Earthquake rupture dependence on hypocentral location along the Nicoya Peninsula subduction megathrust, *Earth Planet. Sci. Lett.* **520,** 10–17, doi: 10.1016/j.epsl.2019.05.030.

Yang, H., S. Yao, B. He, A. V. Newman, and H. Weng (2019). Deriving rupture scenarios from interseismic locking distributions along the subduction megathrust, *J. Geophys. Res.* **124,** 10,376–10,392, doi: 10.1029/2019JB017541.

Yao, S., and H. Yang (2020). Rupture dynamics of the 2012 Nicoya Mw 7.6 earthquake: Evidence for low strength on the Megathrust, *Geophys. Res. Lett.* **47,** e2020GL087508, doi: 10.1029/2020GL087508.

Yin, A., and T. M. Harrison (2000). Geologic evolution of the Himalayan-Tibetan orogen, *Annu. Rev. Earth Planet. Sci.* **28,** 211–280, doi: 10.1146/annurev.earth.28.1.211.

Yu, J., K. Tan, C. Zhang, B. Zhao, D. Wang, and Q. Li (2019). Present-day crustal movement of the Chinese mainland based on global navigation satellite system data from 1998 to 2018, *Adv. Space Res.* **63,** 840–856, doi: 10.1016/j.asr.2018.10.001.

Zhang, P.-Z. (2013). Beware of slowly slipping faults, *Nature Geosci.* **6,** 323–324, doi: 10.1038/ngeo1811.

Zhao, D., C. Qu, R. Bürgmann, W. Gong, and X. Shan (2021). Relaxation of Tibetan lower crust and afterslip driven by the 2001 Mw7.8 Kokoxili, China, earthquake constrained by a decade of geodetic measurements, *J. Geophys. Res.* **126,** e2020JB021314, doi: 10.1029/2020JB021314.

Zheng, G., H. Wang, T. J. Wright, Y. Lou, R. Zhang, W. Zhang, C. Shi, J. Huang, and N. Wei (2017). Crustal deformation in the India-Eurasia collision zone from 25 years of GPS measurements, *J. Geophys. Res.* **122,** 9290–9312, doi: 10.1002/2017JB014465.

Zhu, Y., F. Diao, Y. Fu, C. Liu, and X. Xiong (2021). Slip rate of the seismogenic fault of the 2021 Maduo earthquake in western China inferred from GPS observations, *Sci. China Earth Sci.* doi: 10.1007/s11430-021-9808-0.

Manuscript received 18 August 2021
Published online 1 December 2021